AIAA

AIAA 98-0881

X-34 EXPERIMENTAL AEROHEATING AT MACH 6 AND 10

Scott A. Berry, Thomas J. Horvath, Michael DiFulvio, Christopher Glass, and N. Ronald Merski

NASA Langley Research Center, Hampton, VA 23681

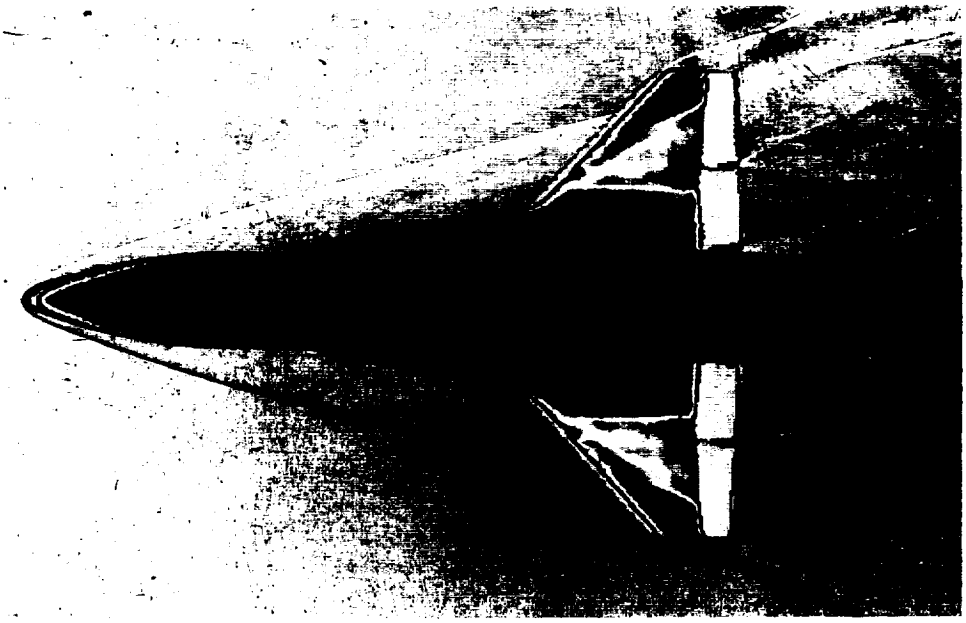

36th AIAA Aerospace Sciences Meeting & Exhibit

January 12-15, 1998 / Reno, NV

X-34 EXPERIMENTAL AEROHEATING AT MACH 6 AND 10

Scott A. Berry*, Thomas J. Horvath*, Michael DiFulvio*, Christopher Glass*†, and N. Ronald Merski*

Abstract

Critical technologies are being developed to support the goals of the NASA Office of Aeronautics and Space Transportation Technology Access to Space initiative for next-generation reusable space transportation systems. From the perspective of aerothermodynamic performance throughout the flight trajectory, the Reusable Launch Vehicle program incorporates conceptual analysis, ground-based testing, and computational fluid dynamics to provide flyable suborbital flight demonstrator vehicles. This report provides an overview of the hypersonic aeroheating wind tunnel test program conducted at the NASA Langley Research Center in support of one of these vehicles, the X-34 small reusable technology demonstrator program. Global surface heat transfer images, surface streamline patterns, and shock shapes were measured on 0.0153- and 0.0183-scale models of proposed X-34 flight vehicles at Mach 6 and 10 in air. The primary parametrics that were investigated include angles-of-attack from 0 to 35 deg. and freestream unit Reynolds numbers from 0.5 to 8 million per foot (which was sufficient to produce laminar, transitional, and turbulent heating data), both with and without control surface deflections. Comparisons of the experimental data to computational predictions are included, along with a discussion of the implications of some of the experimental flow features for the flight vehicle.

*†Nomenclature

h	heat transfer coefficient (lbm/ft^2-sec), $\dot{q}/(H_{aw}-H_w)$
h_{F-R}	reference coefficient using Fay-Ridell calculation to stagnation point of a sphere
H	enthalpy (BTU/lbm)
M	Mach number
P	pressure (psia)
$\dot{q}$	heat transfer rate (BTU/ft^2-sec)
t	time (sec)
Re	unit Reynolds number (1/ft)
T	temperature (°R)
α	angle of attack (deg)
δ	control surface deflection (deg)

Subscripts

∞	free-stream conditions
t1	reservoir conditions
t2	stagnation conditions behind normal shock
aw	adiabatic wall
w	wall
L	reference length
b	reference span
E	elevons only
BF	body flaps only
CS	all control surfaces

Introduction

The Reusable Launch Vehicle (RLV) technology development program, a major component of NASA's Access to Space initiative, has identified key technologies which must be demonstrated before proceeding with the design and implementation of next-generation fully-reusable space transportation systems. In response to this initiative, sub-orbital technology-testbed flight-test demonstrators, the X-33 and X-34 vehicles, are being developed. The X-34 is a winged-body vehicle that is smaller in size and scope, and, thus, lighter and less expensive to build and fly than the X-33 lifting-body vehicle. Intended for hypersonic flight up to Mach 8, the X-34 was conceived to investigate key RLV technologies (such as advanced materials and flight systems, and low-cost operations) which may demonstrate near-term order-of-magnitude reductions in the cost of access to space. A historical review of the early status and objectives of the X-33, X-34, and RLV programs is provided in Ref. 1.

Orbital Sciences Corporation (OSC) has been chosen as the prime contractor for the X-34 program and provides oversight for the vehicle's design, construction, and flight-testing. An overview (although now technically dated) of the X-34 industry/government partnership is provided in Ref. 2. Phase 1 of the X-34 effort involves the design, construction, and supersonic flight testing of a 58 ft. long, rocket-powered vehicle. Phase 2 objectives include expansion of the flight Mach number to 8 with a demonstrated capability to conduct 25 flights in a one year period. The X-34 will be air-launched from OSC's L-1011 airplane. Just after the drop, the single engine is ignited, as is shown in an artist's sketch

* Aerospace Technologist, Aerothermodynamics Branch, Aero- and Gas-Dynamics Division, NASA Langley Research Center, Hampton, VA 23681.

† Member AIAA.

Figure 1 Artist sketch of the X-34 ascent.

in Fig. 1, and the rocket ascends up to an altitude of 250,000 ft. (At this point, an operational RLV version of the X-34 would release the second stage orbital insertion payload.) After an autonomous approach, landing will be on a conventional runway. A typical Mach 8 trajectory is shown in Fig. 2, with peak heating occurring in the vicinity of Mach 6 and a flight length Reynolds number of over 16 million. Based on these flight conditions, the vehicle Thermal Protection System (TPS) will be conservatively designed to heating levels of a fully turbulent boundary layer.

A task agreement between OSC and NASA Langley Research Center (LaRC) has been put into place to help define the X-34 aerothermodynamic environment and assist in the analysis of the TPS design of the vehicle. To meet the objectives of the task agreement, a combined experimental/computational approach has been initiated. Computational Fluid Dynamics (CFD) has been used to predict the aeroheating to the X-34 for two flight cases near the peak heating condition, thus providing the expected maximum surface temperature for selection of TPS material (see Ref. 3). A coupled inviscid/boundary-layer technique was used to compare with CFD results and provide several additional points along the trajectory (detailed in Ref. 4). These results were incorporated with an engineering-type trajectory analysis tool to predict the time history of heating rates for the entire trajectory, thus providing an estimate of the total heat load for over 60 body-points on the vehicle for TPS thickness sizing (see Ref. 5). The wind tunnel program was set up to provide an experimental database over a wide range of parametrics for calibration/validation of the computations.

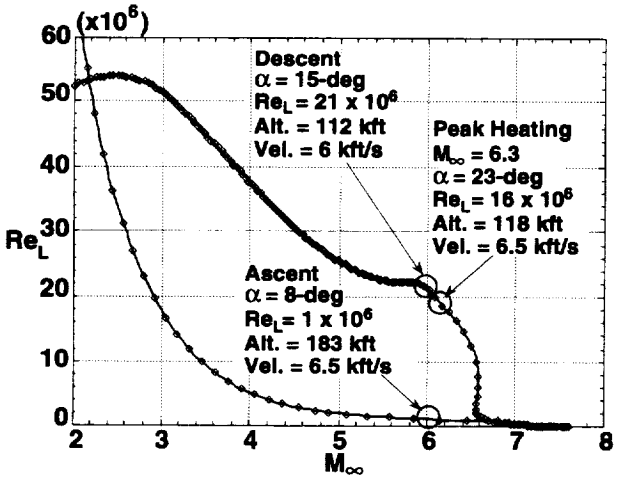

Figure 2 Typical X-34 trajectory.

This paper presents an overview of the experimental measurements made to characterize the X-34 aeroheating environment. These measurements were conducted in the LaRC 20-Inch Mach 6 and 31-Inch Mach 10 Tunnels. Global surface heat transfer distributions, surface streamline patterns, and shock shapes were obtained on two different scale models of the proposed X-34 flight vehicle. Both a 0.0153-scale model of Configuration X0000912 (a preliminary version of the X-34 investigated prior to the freeze of the Outer Mold-Lines (OML) in Dec. 1996) and a 0.0183-scale model of Configuration X0001215, which includes the TPS OML, have been extensively tested. The primary parametrics were angles-of-attack (α) ranging from 0 to 35 deg. and freestream unit Reynolds numbers ranging from 0.5 to 8 million per foot, both with and without control surface deflections. The global heat transfer images were acquired using the phosphor thermography technique[6] which is ideally suited for identifying the heating patterns of complex, three-dimensional flow phenomena. An experimental database was generated from 6 separate test series in 3 LaRC hypersonic facilities, which generated over 280 runs (or datapoints). For the purpose of this paper, a subset of this extensive database will be presented, focusing primarily on the 0.0183-scale model data at the Mach 6 descent condition of α = 15°. (The entire dataset will be documented separately in a series of NASA Technical Memorandums.) Comparisons of the experimental data with CFD and engineering predictions are included, as well as extrapolation of the experimental data to flight conditions.

Experimental Methods

Model Description

A dimensioned sketch of the 0.0183-scale model is shown in Fig. 3. While a rapid prototyping technique was used to build a resin stereolithography model with detachable wing elevons and body flaps for the earlier 0.0153-scale model, the high-fidelity 0.0183-scale model was fabricated out of stainless steel using a numerically controlled milling machine and also had detachable wing

All dimensions are in inches.

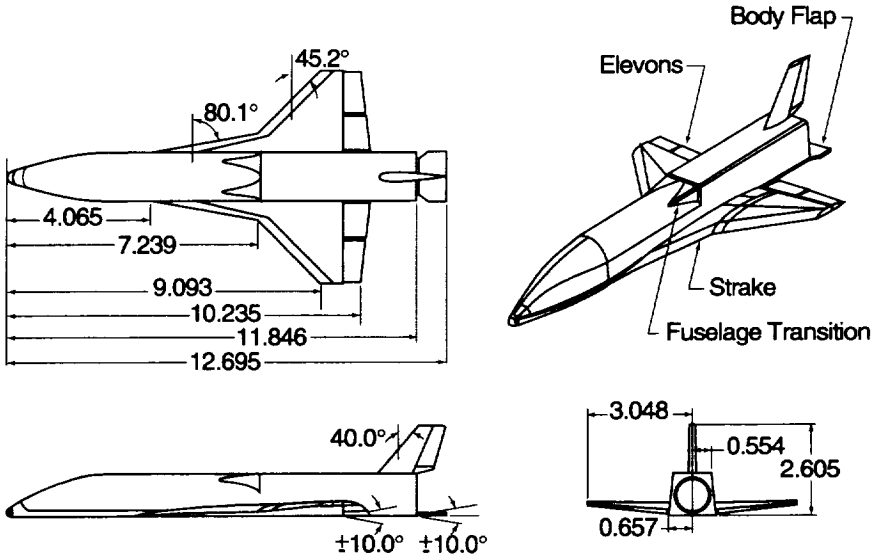

Figure 3 Dimensions for 0.0183-scale X-34 model of Configuration X0001215.

elevons and body flaps. These models were then assembled with the desired control surface settings and used as patterns to create molds from which the ceramic heating models were cast. Several models of each configuration were cast with various control surface deflections and these models are detailed in Table 1. In order to obtain accurate heat transfer measurements with the phosphor thermography technique, which uses the one-dimensional heat conduction equation, the cast models are made of a silica ceramic material with low thermal diffusivity and well defined, uniform, thermal properties. The models were then coated with a mixture of phosphors suspended in a silica-based colloidal binder. The coatings typically do not require refurbishment between runs in the wind tunnel and have been measured to be approximately 0.001 inches thick. For the flow visualization tests, the machined stainless steel model was used.

Facility Description

The X-34 models were tested in the 20-Inch Mach 6 Air and the 31-Inch Mach 10 Air Tunnels of the LaRC Aerothermodynamic Facilities Complex. Detailed descriptions of these facilities and related instrumentation are presented in Refs. 7 and 8. Both are blowdown facilities which utilize dried, heated, and filtered air as the test gas.

The 20-Inch Mach 6 tunnel operates at stagnation pressures ranging from 30 to 500 psia, stagnation temperatures from 410°F to 500°F, and free stream unit Reynolds numbers from 0.5 to $8x10^6$/ft. A two-dimensional, contoured nozzle is used to provide freestream Mach numbers from 5.8 to 6.1. The test section is 20.5 by 20 inches. A bottom-mounted model injection system can insert models from a sheltered position to the tunnel centerline in less than 0.5-sec. Run times up to 15 minutes are possible with this facility, although for the current heat transfer and flow visualization tests run times were only a few seconds. A photograph of a ceramic model (with control surface deflections of zero) installed in the 20-Inch Mach 6 Tunnel for phosphor testing is shown in Fig. 4.

Typical operating conditions for the 31-Inch Mach 10 tunnel are stagnation pressures ranging from 350 to 1450 psia and stagnation temperatures from 1350 to 1450 °F yielding freestream unit Reynolds numbers from 0.5 to $2x10^6$/ft. The tunnel has a closed 31- by 31-in. test section with a contoured three-dimensional water-cooled nozzle to provide Mach numbers from 9.6

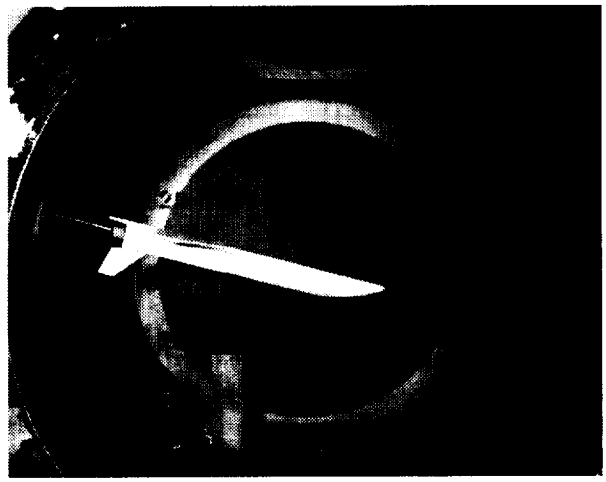

Figure 4 Photograph of ceramic X-34 model installed in LaRC 20-Inch Mach 6 Tunnel.

to 10. A hydraulically operated model injection mechanism can inject the model into the flow in 0.6 seconds. The maximum run time for this facility is approximately 2 minutes; typical run times for heat transfer tests are approximately 5 seconds.

Test Conditions

Nominal reservoir stagnation and corresponding freestream flow conditions for the present study are presented in Tables 2 and 3. Test-section flow conditions in the 20-Inch Mach 6 Air Tunnel were determined from the measured reservoir pressure and temperature and the measured pitot pressure at the test section. Flow conditions for the 31-Inch Mach 10 Air Tunnel were based on measured reservoir pressures and temperatures and recent unpublished calibrations of the facility.

The different model configurations (with and without control surface deflections) were tested over a range of angles of attack (α) from 0 to 35 deg. in roughly 5-deg. increments in both facilities. Also the three trajectory points shown in Fig. 2 (α of 8° for the Mach 6 ascent, α of 15° for the Mach 6 descent, and α of 23° for the peak heating case) were extensively tested. The sideslip angle was maintained at zero for all runs with the exception of a few runs obtained with a sideslip of 4 deg.

Test Techniques

The rapid advances in image processing technology, which have occurred in recent years, have made digital optical measurement techniques practical in the wind tunnel. One such optical acquisition method is two-color relative-intensity phosphor thermography (see Refs. 6, 9, 10, and 11) which is currently being applied to aerothermodynamic testing in the hypersonic wind tunnels of LaRC (for example, see Refs. 12, 13, and 14). With this technique, ceramic wind tunnel models are fabricated and coated with phosphors which fluoresce in two regions of the visible spectrum when illuminated with ultraviolet light. The fluorescence intensity is dependent upon the amount of incident ultraviolet light and the local surface temperature of the phosphors. By acquiring fluorescence intensity images with a color video camera of an illuminated phosphor model exposed to flow in a wind tunnel, surface temperature mappings can be calculated on the portions of the model which are in the field of view of the camera. A temperature calibration of the system conducted prior to the study provides the look-up tables which are used to convert the ratio of the green and red intensity images to global temperature mappings. With temperature images acquired at different times in a wind tunnel run, global heat transfer images are computed assuming one-dimensional heat conduction. Phosphor thermography is routinely used in Langley's hypersonic facilities to obtain quantitative global heat transfer measurements from models that can be fabricated much quicker and more economically than other "more conventional" techniques.

Flow visualization techniques, in the form of schlieren and oil-flow, were used to complement the surface heating tests. The 20-Inch Mach 6 Tunnel is equipped with a pulsed white-light, Z-pattern, single-pass schlieren system with a field of view encompassing the entire 20-in test core. Images were recorded on 70-mm film and digitally scanned for incorporation in this report. The 31-Inch Mach 10 Tunnel does not currently have an operating schlieren system. Surface streamline patterns were obtained using the oil-flow technique in both facilities using the stainless-steel model (spray-painted black to enhance contrast with the white pigmented oils used to trace streamline movement). Oil-flow movement was recorded with a conventional video camera and post-run photographs were recorded with a high-resolution digital camera.

Data Reduction and Uncertainty

Heat transfer coefficients were calculated from the global surface temperature measurements using the IHEAT data reduction code discussed in Ref. 6, assuming one-dimensional heat-conduction to a semi-infinite solid. In determining the heat transfer coefficient, the adiabatic wall enthalpy (H_{aw}) was chosen to be the average between the total enthalpy (H_{t2}) and the calculated adiabatic wall enthalpy on a flat plate at incidence. Heating distributions are presented in terms of the ratio of heat-transfer coefficients h/h_{F-R}, where h_{F-R} corresponds to the Fay and Ridell[15] stagnation-point heating to a sphere with radius 0.09825-in (the full-scale nose radius scaled to the model size) for the 0.0153-scale model and 0.13095-in for the 0.0183-scale model. The heat transfer measurements are estimated to be accurate within ±7-10 percent (and is dependent on the measured surface temperature) in the 31-Inch Mach 10 Tunnel, and only slightly higher in the 20-Inch Mach 6 Tunnel due to a lower total-temperature driver potential.[6] The uncertainty levels reported in the results section are based on the procedure outlined by the AIAA Standards Committee[16] for a 95 percent confidence level. Repeatability for the normalized centerline heat transfer measurements was found to be better than ±4 percent.

Prediction Methods

As part of LaRC's task agreement with OSC, computational predictions of the aeroheating environment using CFD (LAURA) coupled with engineering

codes (LATCH, MINIVER) have been performed to assist in the design of the X-34 flight vehicle. Of the computations that have been completed, most have been applied to predict laminar and turbulent heating rates at flight conditions.[3,4] A few wind tunnel cases have been computed for comparison with the experimental data. To supplement the experimental comparisons, the General Aerodynamic Simulation Program[17, 18] (GASP), another widely-used computational tool, has also been implemented. As details about both LAURA and LATCH can be found in Refs. 3 and 4, respectively, only a discussion of GASP will be included here.

A commercially available software product of AeroSoft, Inc., GASP, is a three-dimensional finite-volume CFD algorithm, which solves the time-dependent, Reynolds averaged Navier-Stokes (RANS) equations. Other subsets of the RANS equations that are available in GASP are: steady, one-dimensional, two-dimensional, axi-symmetric, thin-layer, parabolic space marching, and Euler. A number of physical models from perfect gas to non-equilibrium chemistry and non-equilibrium internal energy for laminar and two-equation turbulence models are available.[18] GASP predicted heating has been validated by comparing with flight Shuttle Orbiter surface measurements during the STS-2 reentry from orbit[19] and then applied to the TPS analysis for the X-33,[20] RLV,[21] and the X-38[22] vehicles.

For the present study, the steady RANS equations were applied by GASP to a X-34 volume grid[23] that was scaled to the appropriate wind tunnel scale. The volume grid was adapted and optimized to the boundary layer and shock wave system that surrounds the configuration using the align-shock subroutine of the LAURA code.[24] Air was modeled as a perfect gas. Viscosity and thermal conductivity were calculated using Sutherland's law. Free stream conditions for the CFD simulation of the wind tunnel condition were matched with the wind tunnel run. Laminar and turbulent solutions were obtained at the nominal flow condition to bound the experimental data, which showed laminar, transitional, and turbulent heating levels. Turbulence was modeled by the algebraic Baldwin-Lomax model.

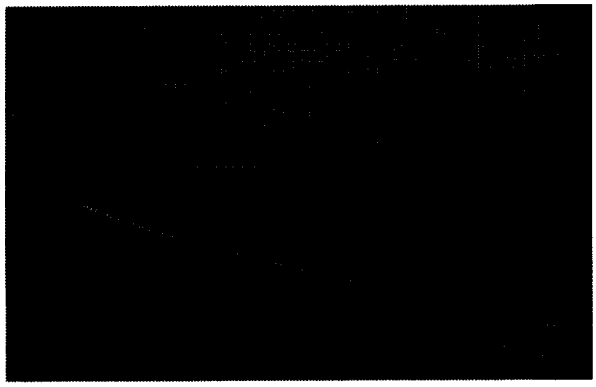

a) Planform view.

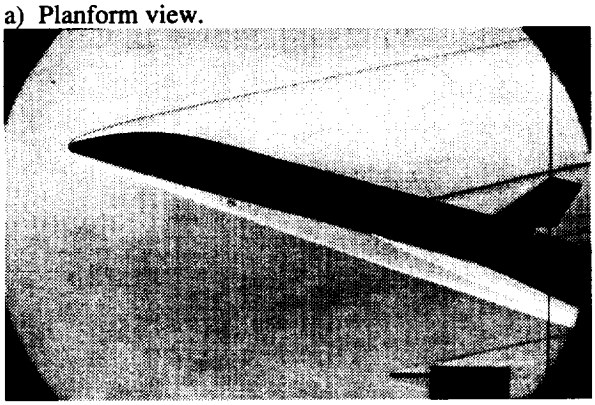

b) Side view.

Figure 5 Schlieren images at $M_\infty = 6$, $\alpha = 15°$, $Re_\infty = 6x10^6$/ft, and $\delta_{CS} = 0°$.

Results and Discussion

Experimental Flow Visualization

The shock shape about the X-34 vehicle for $M_\infty = 6$, $\alpha = 15°$, and control surface deflections (δ_{CS}) of zero is illustrated in Fig. 5. In the planform view, Fig. 5a, the bow shock is shown to interact with the wing leading edge. (Although the data is not shown here, this interaction takes place for all the angles of attack tested.) A cross-section (at the wing/strake juncture) of the computed Mach contours for the flight case of $\alpha = 15°$ and $Re_L = 21x10^6$ (courtesy of Ref. 3) is shown in Fig. 6,

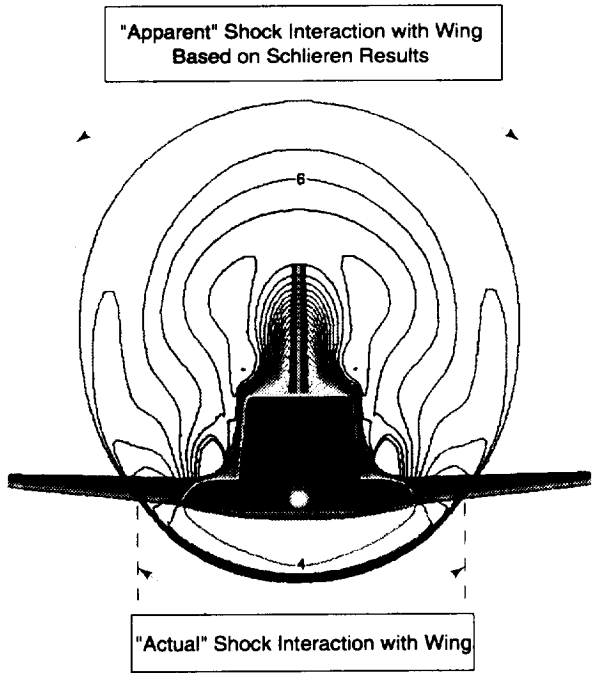

Figure 6 Computational cross-section showing Mach contours at $M_\infty = 6$ and $\alpha = 15°$ (courtesy of Ref. 3).

which shows that the location of shock impingement on wing is actually inboard of the shock shape edge shown in Fig. 5a. This inboard shock interaction location will be shown to agree with the heating and oil-flow results. The side-view schlieren image in Fig. 5b shows a typical bow shock surrounding the vehicle, as well as the shock emanating from the wing leading edge.

Surface streamline patterns from the Mach 6 tunnel at α = 15°, Re_∞ = 4.4x10^6/ft, and δ_{CS} = 20° are shown in Fig. 7. This Reynolds number is sufficiently high enough to produce non-laminar flow, as shown in the windside image (Fig. 7a) where the flow remains attached in front of the deflected control surfaces. (At a lower Re_∞, large laminar separation regions are evident for even relatively small control surface deflections.) The windward surface streamlines first flow inboard near the nose (as shown by the oil-flow build-up on centerline), then outboard once the strake is reached. The highly energized flow associated with the bow shock interaction with the wing is identified by the darkened v-shaped region (near the wing/strake juncture), which results from the white oil being scrubbed away. In Fig. 7b (the portside image) the strake vortex scrubbing on the fuselage is identified by the feather pattern in the oil that leads towards the upper surface fuselage transition (from a D-shaped cross-section to a square). Fig 7c shows the typical leeside reattachment on centerline, and separations in the wing root region.

Similar results were obtained in the Mach 10 tunnel, shown in Fig. 8, for α = 15°, δ_{CS} = 0°, and Re_∞ = 1x10^6/ft. At these conditions, the windward surface flow is laminar. The only significant difference between the Mach 6 and 10 oil-flow results is the slightly more inboard location of the bow shock interaction on the wing for the Mach 10 case.

Experimental Surface Heating

The Mach number effect shown in the oil flows can be also be seen by comparing the windward heat transfer images of Figs. 9 (Mach 6) and 10 (Mach 10). Both are for the X-34 vehicle at α=15°, δ_{CS} =0°, and Re_∞ =1x10^6/ft. At the higher Mach number, the bow shock lies closer to the body and, thus, the interaction with the wing moves further inboard. Both images show that at this condition the windward surface remains laminar. As a side note: by comparing these two images, the lower

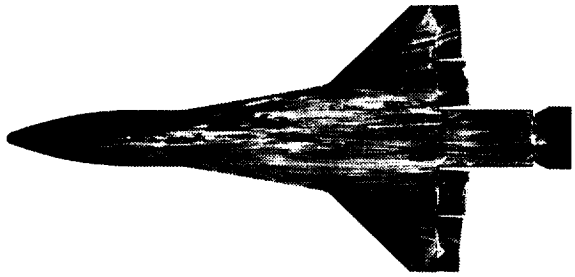

a) Windside view.

b) Portside view.

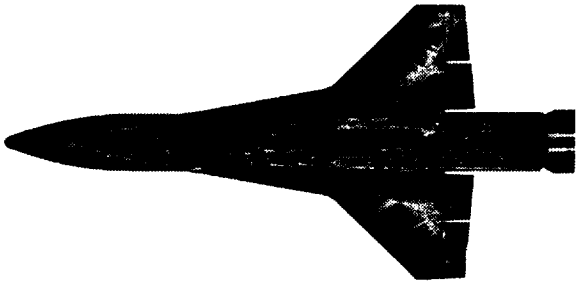

c) Leeside view.

Figure 7 Oil-flow images for M_∞ = 6, α =15°, Re_∞ = 4.4x10^6/ft, and δ_{CS} = 20°.

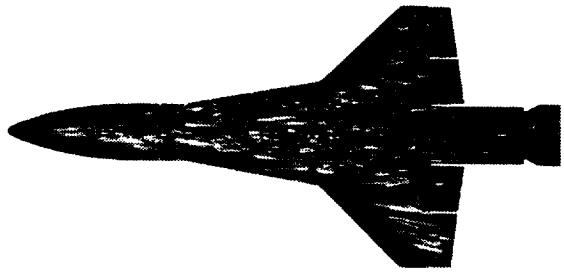

a) Windside view.

b) Portside view.

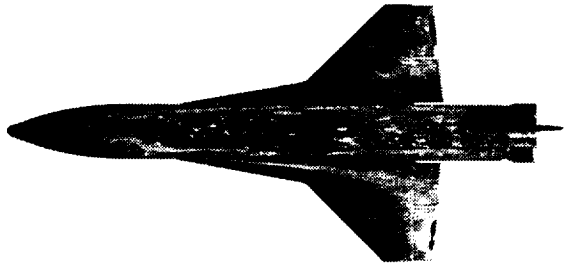

c) Leeside view.

Figure 8 Oil-flow images for M_∞ = 10, α =15°, Re_∞ = 1.1x10^6/ft, and δ_{CS} = 0°.

uncertainty levels associated with the Mach 10 data (due to the higher temperature driver potential) is revealed by the sharper definition of this image.

The effect of angle of attack on the windward surface heat transfer images for freestream conditions of $M_\infty = 6$, $Re_\infty = 1x10^6$/ft, and $\delta_{CS} = 0°$ is shown by comparing Figs. 11 ($\alpha=8°$) and 12 ($\alpha=23°$) to Fig. 9 ($\alpha=15°$). As the angle of attack increases from 8-deg to 23-deg, the windward surface heating increases slightly and bow shock interaction with the wing moves inboard. (Although for the 8-deg case, the heating scale range of 0 to 0.4 tends to hide the weak wing interaction footprint. This scale was dictated by the subsequent heating images for the higher Reynolds numbers.)

The effect of increasing Reynolds number on the windward surface heating images at Mach 6, $\alpha=15°$, and $\delta_{CS} = 0°$ is shown in Figs. 9, 13, 14 and 15. The windward surface remains laminar at the lowest Reynolds number (Fig. 9). As the Reynolds number increases to 2 million per foot (Fig 13), boundary-layer transition first occurs along the centerline, as illustrated by the higher heating region (transition front) on the aft fuselage. Then, at $Re_\infty = 4x10^6$/ft (Fig. 14), transition begins to affect the bow/wing shock interaction region and moves further forward on centerline. Finally, at $Re_\infty = 7.9x10^6$/ft (Fig. 15), the entire rear half of the windward surface is non-laminar. While the location of transition in the wind tunnel cannot be used as an indicator of the actual location of transition in flight (because of tunnel related flow disturbances), the relative ease with which the windward surface boundary layer flow transitions, when compared to other vehicles tested in these facilities (Shuttle, X-33, X-38, etc.), tends to suggest a potential for early transition for the X-34 flight vehicle. The decision to conservatively design the TPS for a fully turbulent boundary layer appears appropriate.

The effect of control surface deflections on the windward surface heating for the turbulent case is shown by comparing Fig. 15 ($\delta_{CS} = 0°$) to Fig. 16 ($\delta_{CS} = 10°$). Both are for the X-34 vehicle at Mach 6, $\alpha=15°$, and $Re_\infty = 7.9x10^6$/ft. These images can be used to determine the turbulent heating augmentation levels due to the deflected control surfaces. With the baseline deflection of zero, heating levels on the order of 0.10 to 0.18 of the stagnation point reference are evident on the control surfaces; for the $\delta_{CS} = 10°$ case, the heating levels approach 0.18 to 0.34 the stagnation point reference. This averages out to roughly a doubling of the heat transfer coefficient for a 10° control surface deflection.

Computational Comparisons

The results of the GASP and LAURA[3] computations for the wind tunnel conditions of Mach 6, $\alpha=15°$, $\delta_{CS} = 0°$, and $Re_\infty = 7.9x10^6$/ft, along with a comparison to the experimental data, are shown in Figs. 17 and 18, respectively. The laminar predictions for GASP (Fig. 17a) and LAURA (Fig. 18a) compare favorably to the experimental results for most of the forebody. The turbulent predictions (Figs. 17b and 18b) match the experimental data for the remainder of the forebody, wings, and aftbody. There are subtle differences between the two solutions and the experimental data on the wing, perhaps due to a lack of grid resolution in the shock interaction region. Figure 19 provides a comparison of the heating distributions along the centerline between GASP, LAURA,[3] LATCH,[4] and the experimental data. All the computations are for the same wind tunnel case. There is excellent agreement between the experimental data and the predictions for the laminar portion. In the turbulent region, the experimental data agrees best with the LAURA predictions. These comparisons provide a great deal of confidence about the validity of both the experimental and computational results.

Extrapolation to Flight

A relatively new feature of the phosphor thermography test technique is the ability to extrapolate the experimental images to flight conditions. Details of this new feature are found in Ref. 6. An example of the results of both a laminar and turbulent extrapolation of wind tunnel data to flight conditions is presented in Fig. 20, with a comparison to LAURA flight calculations of the equilibrium radiative wall temperature. (Note that these results are for the peak heating case of $\alpha=23°$, instead of the $\alpha=15°$ cases discussed earlier. The LAURA flight calculations of Ref. 3 had laminar predictions for the peak heating $\alpha=23°$ case only.) The favorable comparison between the extrapolated wind tunnel results and flight predictions provides confidence about the validity of the extrapolation technique.

Another technique often used to extract flight relevant information from wind tunnel data is to derive empirical correlations (or factors) that when coupled with analytic solutions can provide reasonable estimates of the effects of important parameters in flight. The Mach 6 experimental dataset was used to obtain control surface deflection augmentation factors for the turbulent case and these results are shown in Fig. 21, along with the estimated uncertainty levels. Data from the three trajectory points of $\alpha=8°$, $\alpha=15°$, and $\alpha=23°$, as well as all the control surface deflections (using both configurations) tested (δ_{CS} = -10°, 0°, 5°, 10°, and 20°) are included. The current limit for control surface deflections on descent is $\delta_{CS} = 10°$, which, based on these empirical relations, would roughly double the heating to the control surfaces.

Finally, these wind tunnel results can be used to provide guidance in regards to potential high-heating trouble spots for the flight vehicle. For instance, on the windward surface there were three regions, aside from the expected bow shock interaction region on the wing leading edge, that consistently showed elevated heating levels: the outboard gap between the two elevons, which has shown to be one of the hottest spots on the model during a run; the inboard elevon which typically must endure the effect of the highly energized flow of the wing shock interaction; and the sides of the "cut-out" region on the body flap. These three spots are illustrated in the heating image of Fig. 22, which was generated by zooming the phosphor thermography system in close to look for fine details and corresponds to the case shown in Fig. 16. On the leeside, the tail leading edge and the fuselage transition are the regions that showed the most heating.

Concluding Remarks

An overview of the hypersonic aeroheating wind tunnel test program conducted at the NASA Langley Research Center in support of the X-34 small reusable technology demonstrator program is presented. Global surface heat transfer distributions, surface streamline patterns, and shock shapes were measured on 0.0153- and 0.0183-scale models of the proposed X-34 flight vehicle at Mach 6 and 10 in air. The primary parametrics that were investigated include angles-of-attack from 0 to 35 deg. and freestream unit Reynolds numbers from 0.5 to 8 million per foot, both with and without control surface deflections. This Reynolds number range was sufficient to produce laminar, transitional, and turbulent boundary layers. The experimental database that was generated includes effects of Mach number, Reynolds number, configuration changes, angle of attack, and control surface deflections. Analysis of the experimental data verifies that the decision to conservatively design the TPS for a fully turbulent boundary layer appears appropriate. Also, the results provided insight regarding the potential high-heating regions for the flight vehicle, such as the gap between the elevons, the inboard elevon, and the cut-out on the body-flap. Comparisons of the experimental results to computational predictions were performed and agreed with the LAURA results within 10 percent for both laminar and turbulent conditions. Also, these results were used to validate, by comparing with flight computations, an extrapolation technique that can be used in future applications to directly provide flight information from wind tunnel data.

Acknowledgments

The following individuals were critical to the successful completion of this work: Mark Cagle, Joe Powers, Mark Griffin, Mike Powers, Rhonda Manis, Grace Gleason, Johnny Ellis, Jeff Warner, Larry Murray, Bert Senter, Sheila Wright, Glenn Bittner, Steve Alter, Bill Wood, Lisa Brilliant, and Richard Wheless. The authors greatly appreciate their contributions.

References

1. Freeman, D. C., Jr., Talay, T. A., and Austin, R. E., "Single-Stage-to-Orbit---Meeting the Challenge," *Acta Astronautica*, Vol. 38, No. 4-8, 1996, pp. 323-331.
2. Elias, A. L., Hays, D., and Kennedy, J., "Pioneering Industry/Government Partnerships - X-34," AIAA Paper 95-3777, Sept. 1995.
3. Kleb, W. L., Wood, W. A., and Alter, S. J., "Computational Aeroheating Predictions for X-34," AIAA Paper 98-0879, Jan. 1998.
4. Riley, C. J., Kleb, W. L., and Alter, S. J., "Aeroheating Predictions for X-34 Using an Inviscid-Boundary Layer Method," AIAA Paper 98-0880, Jan. 1998.
5. Wurster, K. E., Riley, C. J., and Zoby, V., "Engineering Aerothermal Analysis for X-34 Thermal Protection Design," AIAA Paper 98-0882, Jan. 1998.
6. Merski, N. R., "Reduction and Analysis of Phosphor Thermography Data with the IHEAT Software Package," AIAA Paper 98-0712, Jan. 1998.
7. Miller, C. G., "Langley Hypersonic Aerodynamic/Aerothermodynamic Testing Capabilities - Present and Future," AIAA Paper 90-1376, June 1990.
8. Micol, J. R., "Hypersonic Aerodynamic/ Aerothermodynamic Testing Capabilities at Langley Research Center: Aerothermodynamic Facilities Complex," AIAA Paper 95-2107, June 1995.
9. Buck, G. M., "Automated Thermal Mapping Techniques Using Chromatic Image Analysis," NASA TM 101554, April 1989.
10. Buck, G. M., "Surface Temperature/Heat Transfer Measurement Using A Quantitative Phosphor Thermography System," AIAA Paper 91-0064, Jan. 1991.
11. Merski, N. R., "A Relative-Intensity Two-Color Phosphor Thermography System," NASA-TM-104123, Sept. 1991.
12. Horvath, T. J., Rhode, M. N., and Buck, G. M., "Aerothermodynamic Measurements on a Proposed Assured Crew Return Vehicle (ACRV) Lifting Body Configuration at Mach 6 and 10 in Air," AIAA Paper 90-1744, June 1990.
13. Micol, J. R., "Aerothermodynamic Measurement and Prediction for a Modified Orbiter at Mach 6 and 10 in Air," *Journal of Spacecraft and Rockets*, Vol. 32, No. 5, 1995, pp. 737-748.

14. Berry, S. A., Bouslog, S. A., Brauckmann, G. J., and Caram, J. M., "Boundary-Layer Transition Due to Isolated Roughness: Shuttle Results From the LaRC 20-Inch Mach 6 Tunnel," AIAA Paper 97-0273, Jan. 1997.
15. Fay, J. A., and Ridell, F. R., "Theory of Stagnation Point Heat Transfer in Dissociated Air," *Journal of Aeronautical Sciences*, Vol. 25, No. 2, 1958.
16. Anon., "Assessment of Wind Tunnel Data Uncertainty," AIAA Publication S-071, 1995.
17. McGrory, W. D., Slack, D. C., Applebaum, M. P., and Walters, R. W., "GASP Version 2.2 The General Aerodynamic Simulation Program," AeroSoft, Inc., 1993.
18. AeroSoft, "GASP Version 3, The General Aerodynamic Simulation Program, Computational Flow Analysis Software for the Scientist and Engineer, User's Manual," AeroSoft, Inc., Blacksburg, Virginia, May 23, 1996.
19. Olynick, D. R. and Tam, T., "Trajectory Based Validation of the Shuttle Heating Environment," *Journal of Spacecraft and Rockets*, Vol. 34, No. 2, 1997, pp. 172-181.
20. Gnoffo, P. A., Weilmuenster, K. J., Hamilton, H. H., II, Olynick, D. R., and Venkatapathy, E., "Computational Aerothermodynamics Design Issues for Hypersonic Vehicles," AIAA Paper 97-2473, June 1997.
21. Olynick, D. R. and Henline, W. D., "Navier-Stokes Heating Calculations for Benchmark Thermal Protection System Sizing," *Journal of Spacecraft and Rockets*, Vol. 33, No. 6, 1996, pp. 807-814.
22. Loomis, M. P., Venkatapathy, E., Papadopoulos, P., Davies, C. B., Berry, S. A., Horvath, T. J., and Campbell, C., "Aeroheating and Aerodynamic CFD Validation and Prediction for the X-38 Program," AIAA Paper 97-2478, June 1997.
23. Alter, S. J., "Surface Modeling and Grid Generation of Orbital Sciences X-34 Vehicle (Phase I)," NASA CR-97-206243, Nov. 1997.
24. Cheatwood, F. M. and Gnoffo, P. A., "User's Manual for the Langley Aerothermodynamic Upwind Relaxation Algorithm (LAURA)", NASA TM-4674, April 1996.

Table 1. X-34 Model Configurations.

Configuration #	Model Scale	δ_{BF}	δ_E
A-1	0.0153	0	-4
A-2	0.0153	20	16
A-3	0.0153	0	16
A-4	0.0153	20	-4
B-1	0.0183	0	0
B-2	0.0183	5	5
B-3	0.0183	10	10
B-4	0.0183	-10	-10

Table 2. Nominal Flow Conditions for LaRC 20-Inch Mach 6 Tunnel.

$Re_\infty(x10^6/ft)$	M_∞	P_{t1} (psi)	T_{t1} (°R)	H_{t1}(BTU/lbm)	P_{t2}(psi)
0.59	5.84	29.8	861.7	207.2	0.99
1.15	5.88	60.3	880.8	212.0	1.95
2.23	5.94	125.1	906.7	218.2	3.88
4.40	5.98	250.7	906.2	218.1	7.52
7.95	6.02	475.0	925.0	222.6	13.88

Table 3. Nominal Flow Conditions for LaRC 31-Inch Mach 10 Tunnel.

$Re_\infty(x10^6/ft)$	M_∞	P_{t1} (psi)	T_{t1} (°R)	H_{t1}(BTU/lbm)	P_{t2}(psi)
0.6	9.68	347.3	1768	442.1	1.199
1.1	9.78	721.3	1821	457.3	2.357
2.2	9.93	1452.0	1820	458.1	4.506

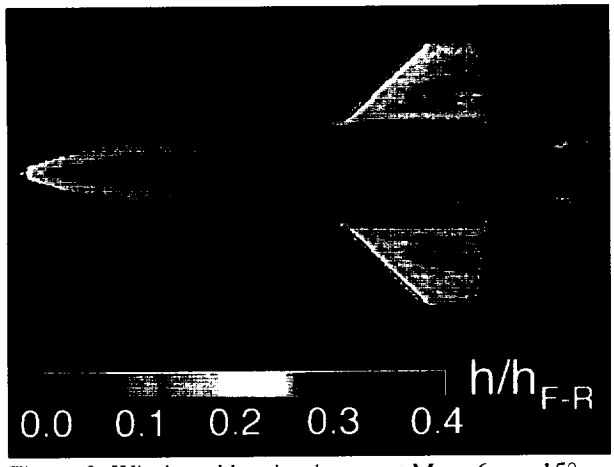

Figure 9 Windward heating image at $M_\infty = 6$, $\alpha = 15°$, $Re_\infty = 1.1 \times 10^6$/ft, and $\delta_{CS} = 0°$.

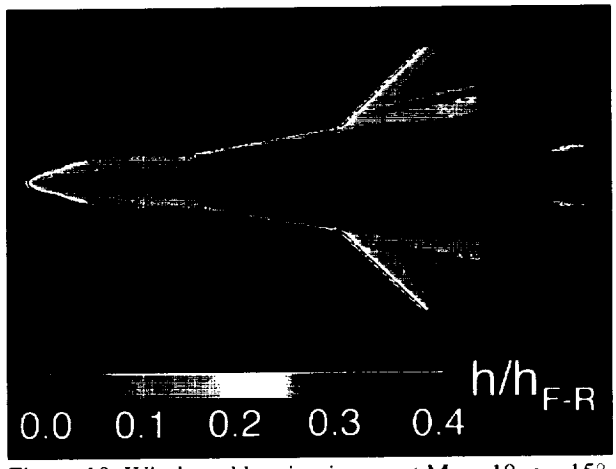

Figure 10 Windward heating image at $M_\infty = 10$, $\alpha = 15°$, $Re_\infty = 1.1 \times 10^6$/ft, and $\delta_{CS} = 0°$.

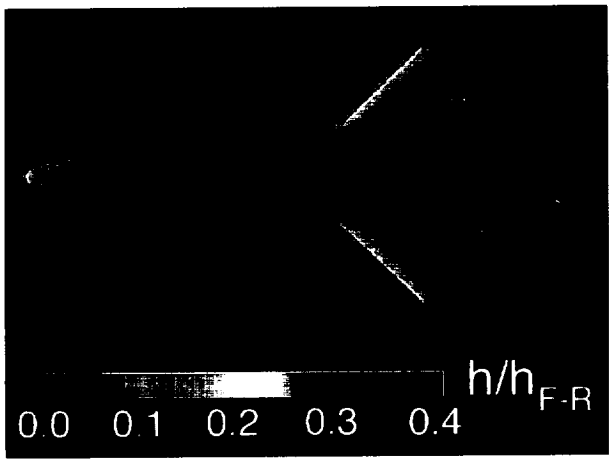

Figure 11 Windward heating image at $M_\infty = 6$, $\alpha = 8°$, $Re_\infty = 1.1 \times 10^6$/ft, and $\delta_{CS} = 0°$.

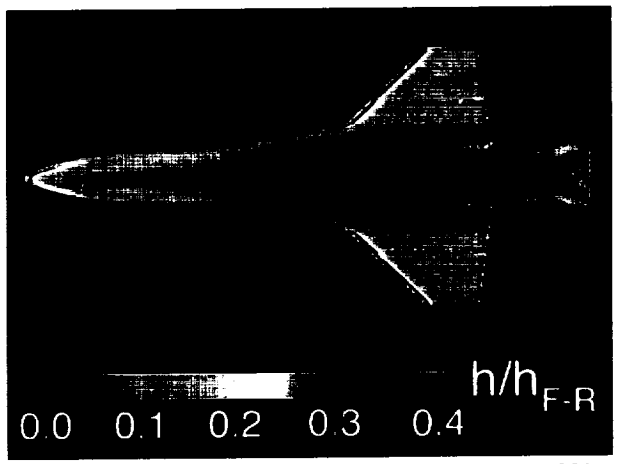

Figure 12 Windward heating image at $M_\infty = 6$, $\alpha = 23°$, $Re_\infty = 1.1 \times 10^6$/ft, and $\delta_{CS} = 0°$.

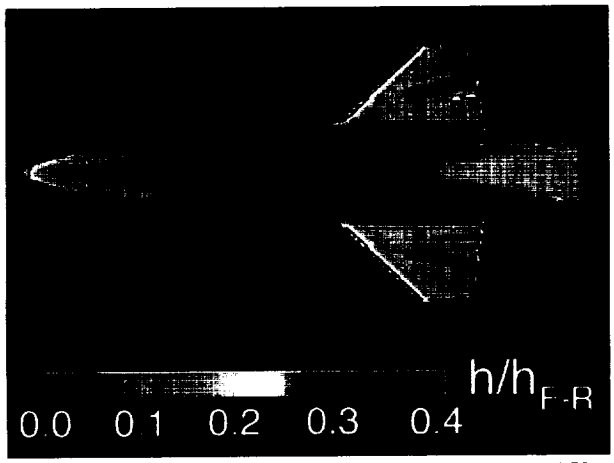

Figure 13 Windward heating image at $M_\infty = 6$, $\alpha = 15°$, $Re_\infty = 2.2 \times 10^6$/ft, and $\delta_{CS} = 0°$.

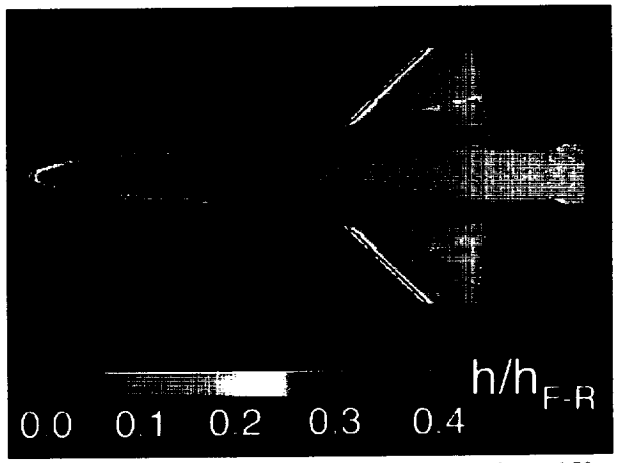

Figure 14 Windward heating image at $M_\infty = 6$, $\alpha = 15°$, $Re_\infty = 4.4 \times 10^6$/ft, and $\delta_{CS} = 0°$.

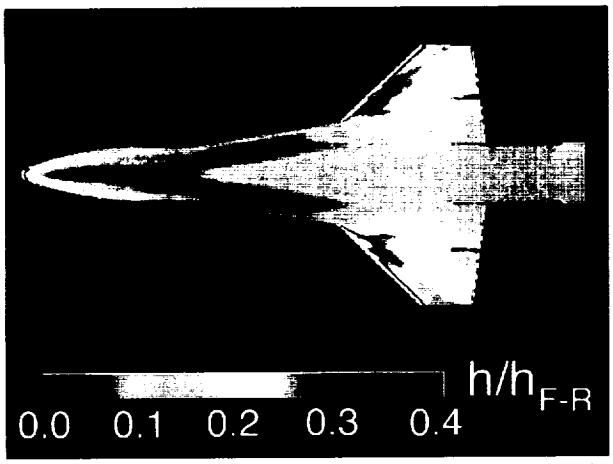

Figure 15 Windward heating image at $M_\infty = 6$, $\alpha = 15°$, $Re_\infty = 7.9x10^6$/ft, and $\delta_{CS} = 0°$.

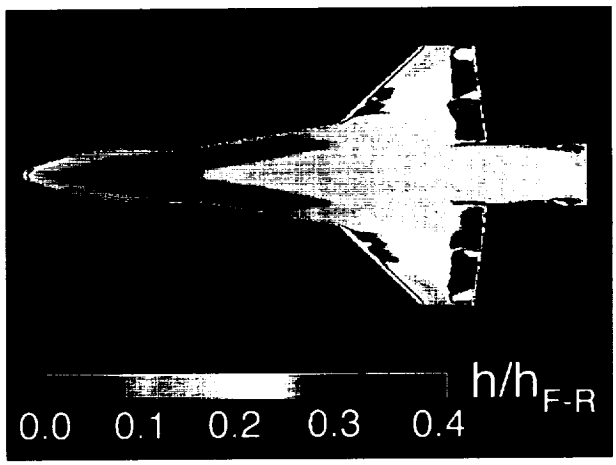

Figure 16 Windward heating image at $M_\infty = 6$, $\alpha = 15°$, $Re_\infty = 7.9x10^6$/ft, and $\delta_{CS} = 10°$.

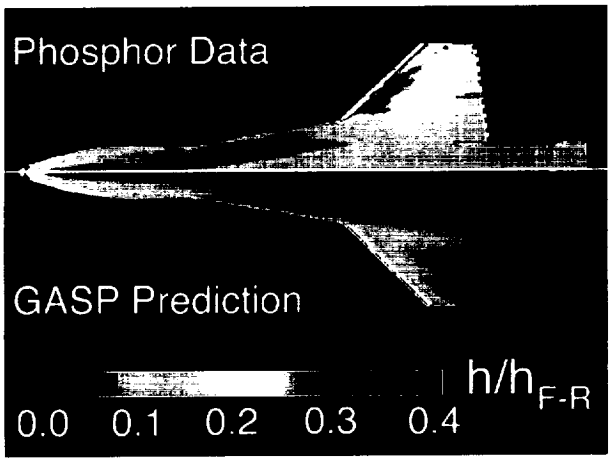

a) Laminar results.

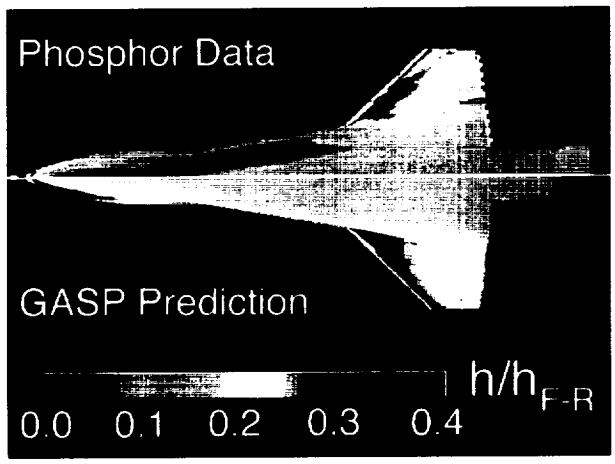

b) Turbulent results.

Figure 17 Comparison of GASP predictions to experimental data at $M_\infty = 6$, $\alpha = 15°$, $Re_\infty = 7.9x10^6$/ft, and $\delta_{CS} = 0°$.

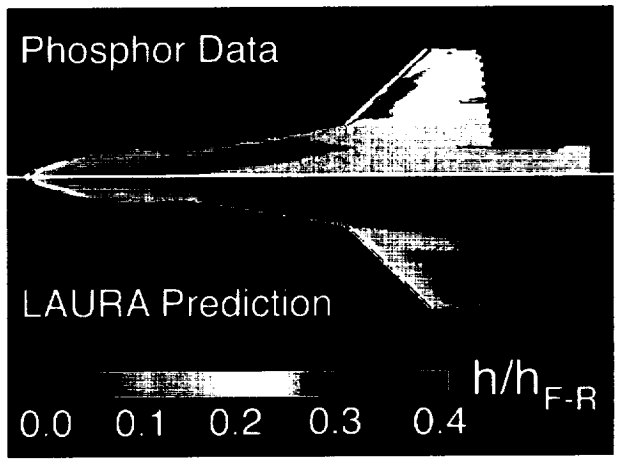

a) Laminar results.

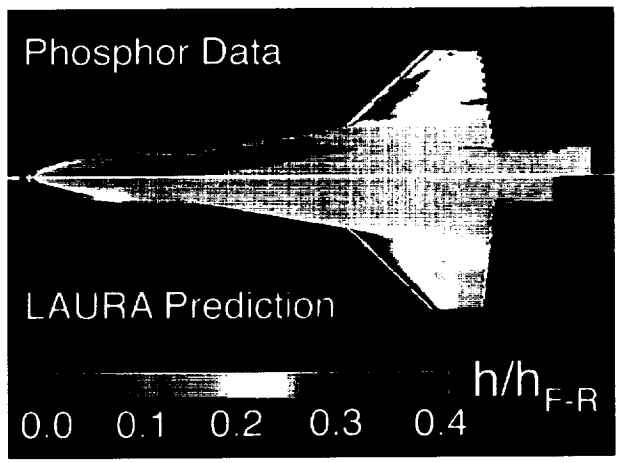

b) Turbulent results.

Figure 18 Comparison of LAURA predictions to experimental data at $M_\infty = 6$, $\alpha = 15°$, $Re_\infty = 7.9x10^6$/ft, and $\delta_{CS} = 0°$.

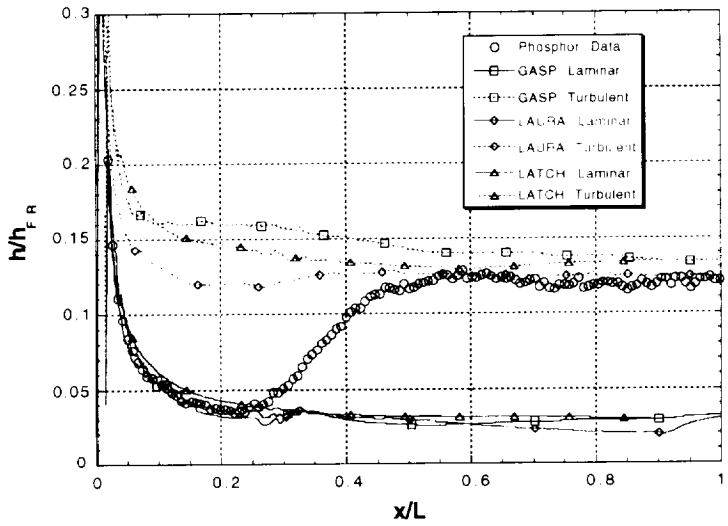

Figure 19 Centerline comparison of computational predictions to experimental data at $M_\infty = 6$, $\alpha = 15°$, $Re_\infty/ft = 7.9x10^6$, and $\delta_{CS} = 0°$.

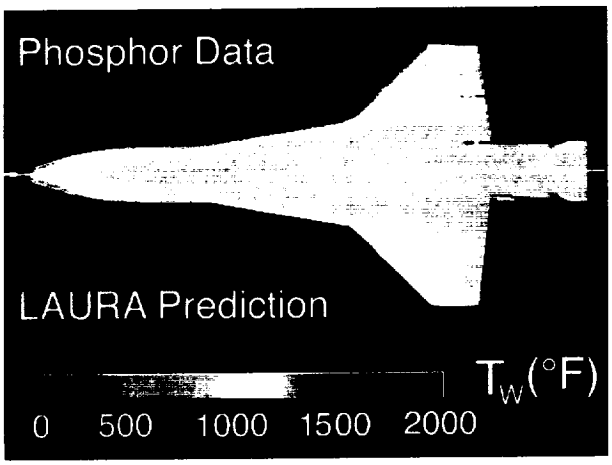

a) Laminar results.

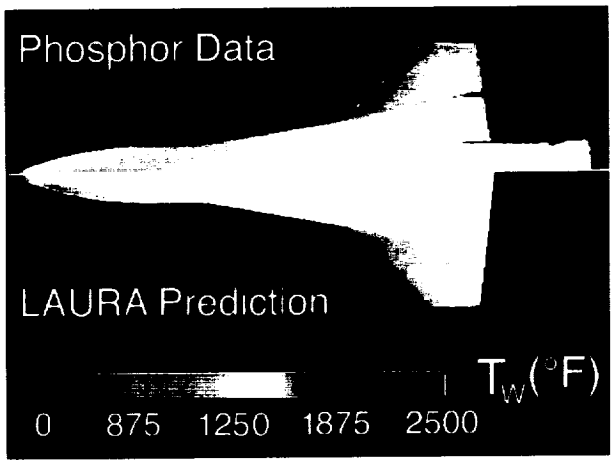

b) Turbulent results.

Figure 20 Extrapolation of experimental data to flight conditions at peak heating ($M_\infty = 6.3$, $\alpha = 23°$, $Re_\infty L = 16x10^6$, and $\delta_{CS} = 0°$).

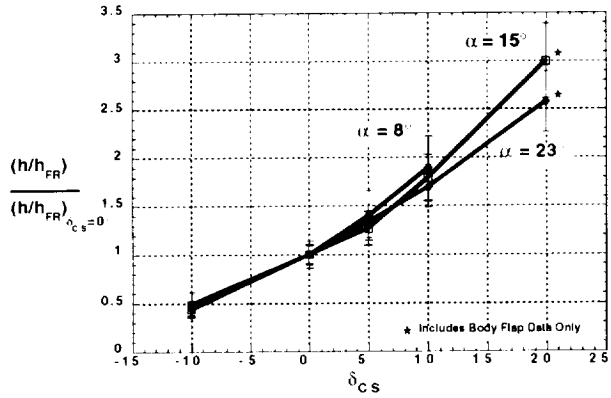

Figure 21 Turbulent control-surface deflection factors from experimental data at $M_\infty = 6$ and $Re_\infty/ft = 7.9x10^6$.

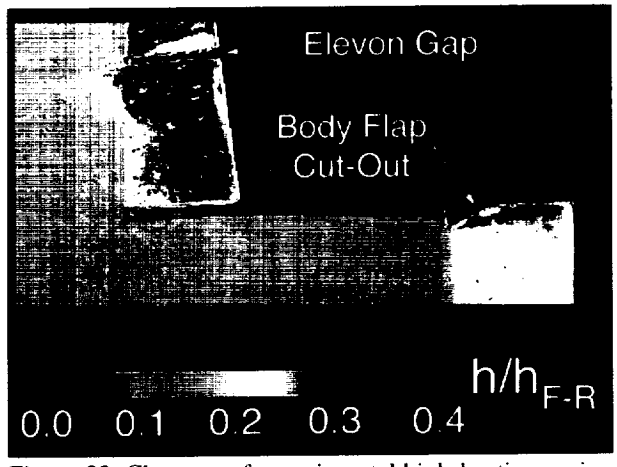

Figure 22 Close-up of experimental high-heating regions of the windward surface for $M_\infty = 6$, $\alpha = 15°$, $Re_\infty/ft = 7.9x10^6$, and $\delta_{CS} = 10°$.